# Probing the Plasma Tail of Interstellar Comet 2I/Borisov

P K Manoharan, Phil Perillat, C J Salter, Tapasi Ghosh, Shikha Raizada, Ryan S Lynch, Amber Bonsall-Pisano, B C Joshi, Anish Roshi, Christiano Brum, And Arun Venkataraman

Arecibo Observatory, University of Central Florida, HC3 Box 53995, Arecibo, PR 00612, USA
 <sup>2</sup>Green Bank Observatory, P.O. Box 2, Green Bank, WV 24944, USA
 <sup>3</sup>National Centre for Radio Astrophysics, Tata Institute of Fundamental Research, Pune 411007, India

#### ABSTRACT

We present an occultation study of compact radio sources by the plasma tail of interstellar Comet 2I/Borisov (C/2019 Q4) both pre- and near-perihelion using the Arecibo and Green Bank radio telescopes. The interplanetary scintillation (IPS) technique was used to probe the plasma tail at P-band (302–352 MHz), 820 MHz, and L-band (1120–1730 MHz). The presence and absence of scintillation at different perpendicular distances from the central axis of the plasma tail suggests a narrow tail of less than 6 arcmin at a distance of  $\sim 10$  arcmin ( $\sim 10^6$  km) from the comet nucleus. Data recorded during the occultation of B1019+083 on 31 October 2019 with the Arecibo Telescope covered the width of the plasma tail from its outer region to the central axis. The systematic increase in scintillation during the occultation provides the plasma properties associated with the tail when the comet was at its pre-perihelion phase. The excess level of L-band scintillation indicates a plasma density enhancement of  $\sim 15$ –20 times that of the background solar wind. The evolving shape of the observed scintillation power spectra across the tail from its edge to the central axis suggests a density spectrum flatter than Kolmogorov, and that the plasma-density irregularity scales present in the tail range between 10 and 700 km. The discovery of a high-frequency spectral excess, corresponding to irregularity scales much smaller than the Fresnel scale, suggests the presence of small-scale density structures in the plasma tail, likely caused by interaction between the solar wind and the plasma environment formed by the comet.

Keywords: comets, individual (2I/Borisov C/2019 Q4) – plasma tail – – occultation – turbulence – scintillation – interplanetary medium

## 1. INTRODUCTION

Cometary nuclei predominantly consist of highly concentrated primordial ices, rock and dust that originated in the very outer regions of a planetary system. They can thus supply information on the early history of such systems. As they approach the Sun, the nuclei of solar-system comets develop gravitationally-unbound atmospheres, or comae, surrounding their nuclei. These comae have diameters many times those of the nuclei, which are typically  $\sim 1-10$  km. Moreover, spectacular tails, formed as comets approach the Sun, are much longer and wider than the comae, sometimes extending up to 1 AU in length. Investigations of these tails are important for understanding the interplanetary processes involved as a comet passes close to the Sun.

Two types of comet tails are formed. Firstly, a dust (or type-2) tail caused by solar radiation pressure, combined with magneto-hydrodynamic forces, which triggers sublimation processes beneath the outer surface of the coma, followed by the supersonic flow of dust particles from the cometary coma/nucleus. A second plasma (or ion) tail, also known as the type-1 tail, is caused by the complex

Corresponding author: P K Manoharan mano@naic.edu, Periasamy.Manoharan@ucf.edu

interaction between the solar wind and the coma through a combination of photo-dissociation of molecules via solar extreme-ultraviolet radiation and charge exchange with the energetic solar-wind plasma. The charged particles gyrate around the frozen-in interplanetary magnetic field and move along the field lines in the anti-solar direction. The plasma tails have opening angles of a few degrees, and are mostly observed to be longer than the dust tails. In fact, the actual size of a plasma tail can be much longer than the structure that is visible optically (Brandt 1968). A plasma tail contains density irregularities that flow out from the coma, and the associated electron-density inhomogeneities scatter the plane radio wave-front from a compact background radio source passing through it causing scintillation to be observed in the intensity of the radio source. (e.g., Brandt 1968; Biermann et al. 1967; Roy et al. 2007).

The measured scintillations as the line of sight to a radio source crosses the plasma tail of a comet can be used to study the properties of that tail. Such studies successfully probed the enhancement of scintillation caused by the tail plasma of several solar-system comets at different distances from the Sun. In particular, Comet Wilson 1987 and Schwassmann-Wachmann 3-B showed the presence of large-scale (∼500 km) and small-scale (≤50 km) density structures at the edge of the tail and near the tail axis respectively (Ananthakrishnan et al. 1975; Alurkar et al. 1986; Hajivassiliou & Duffett-Smith 1987; Slee et al. 1990; Roy et al. 2007). Similarly, "Interplanetary Scintillations" (IPS) occur when the continuum radio emission from a distant compact radio source passes through the small-scale electron density inhomogeneities in the ionized solar-wind plasma. Although originally much used for detecting compact components in distant radio sources, IPS has also long been employed to study both the solar wind, and "coronal mass ejections" moving rapidly outward from the Sun (e.g., Kojima & Kakinuma 1987; Coles 1995; Manoharan et al. 2001).

Comet 2I/Borisov was only the second interstellar object known to have entered the solar system. The first such object, 'Oumuamua' (1I/2017 U1), was a tiny,  $\leq 1 \text{ km} \times \sim 100 \text{ m}$ , elongated, asteroid-like object that appeared inactive even at a perihelion distance of  $\sim 35 \times 10^6 \text{ km}$  (0.23 AU). The highly-eccentric, hyperbolic orbits of these two objects, and their high inclinations to the ecliptic plane, demonstrates that they have an extra-solar system origin. In contrast to 1I/2017 U1, although also small, 2I/Borisov was an active object. Well before perihelion at  $\sim 2 \text{ AU}$  it manifested an elongated coma, indicating the occurrence of jets, with the presence of cyanide and other molecules typically detected from solar-system comets (e.g., Manzini et al. 2020; Cordiner et al. 2020). As 2I/Borisov approached the Sun, solar radiation heated its coma, resulting in the formation of a tail, which grew steadily in length. In late October 2019, the observable dust tail stretched out from the 1 km-sized nucleus to a radial size of  $\sim 2 \times 10^5 \text{ km}$ , corresponding to an angular distance of more than 2 arcmin. Figure 1 displays an image of 2I/Borisov taken with the W.M. Keck Observatory Low-Resolution Imaging Spectrometer on 24 November 2019, when the comet was 2 AU from the Sun, along with an image of the Earth to show the size scale.

Polarimetric observations of 2I/Borisov suggested a remarkably smooth, pristine coma with a high concentration of carbon monoxide, that had likely never interacted with the solar wind of either the Sun or any other star (e.g., Bagnulo et al. 2021). Such comets are particularly interesting because their material is presumably the same as when our solar system and the extra-solar system of 2I/Borisov were formed. Understanding their properties, including the formation of their tails, is important. At the Arecibo and Green Bank Observatories, we took advantage of the passage of the plasma tail of 2I/Borisov in front of a number of compact extragalactic radio sources to attempt investigation of the properties of its plasma tail using radio scintillation observations, at P-band (302–352 MHz), 820 MHz, and L-band (1120–1730 MHz). These observations were unique in determining the dimensions of the plasma tail of 2I/Borisov when it was  $\sim$ 2 AU away from the Earth, assessing the level of its density fluctuations, and deriving the spectrum of its density turbulence, as well as the associated density scale sizes existing across the tail from the edge to the central axis. The wide bandwidths employed in these observations led to high sensitivity, which was an essential requirement in probing the weak level of density fluctuations associated with the small-scale density structures,  $\lesssim 10$  km, near the axis of the plasma tail. In Section 2 we briefly summarize the theory of scintillations introduced into the radio emission from a compact radio source by an intervening plasma screen, and discuss

the parameters of the screen that can be derived from single-dish observations. Section 3 details the orbit of Comet 2I/Borisov, and source selection for our observations. Section 4 provides detailed information of the observations and data analysis. It also presents the results, which are discussed in terms of what they tell us about the plasma tail of 2I/Borisov. Section 5 discusses these results and compares them with our existing knowledge of solar-system comet plasma tails.

## 2. REMOTE SENSING BY SCINTILLATION MEASUREMENTS

#### 2.1. Scintillation Index

Electron density irregularities,  $(\delta n_e)$ , in the out-flowing solar wind plasma, causes scattering of radio waves, which together with the motion of the irregularities across the line of sight to a compact radio source, cause fluctuations in the apparent source intensity. These so-called "interplanetary scintillations" (IPS) are quantified by the fluctuations of the intensity about its mean,  $\delta I(t) = I(t) - \langle I(t) \rangle$ , where I(t) and  $\langle I(t) \rangle$  are the source intensity at time, t, and its average level. The scintillation index, m, is the rms of the intensity fluctuations normalized by the mean source intensity (e.g., Hewish et al. 1964; Manoharan 1993). Scattering is considered to be "strong" if the rms fluctuations imposed on a passing radio wavefront by the medium is  $\Delta \phi > 1$  rad. Otherwise, the scattering is considered to be "weak". For the line-of-sight to an ideal point source, the weak-scattering regime sets in at meter wavelengths at a perpendicular heliocentric distance to the line of sight to a radio source of  $\sim 0.2$  AU, beyond which the value of m decreases (e.g., Cohen & Gundermann 1969; Manoharan 1993). This "strong-to-weak scattering transition" region moves closer to the Sun at higher observing frequency. In the weak-scattering regime, the overall effect on the emission from a source passing through the solar wind can be calculated by linearly adding the contributions from several thin layers (the first Born approximation). Additionally, in such a situation, the scintillation index m is proportional to the plasma density fluctuations  $(\delta n_e)$ , which in turn is related to the density  $(n_e)$  of the solar wind (e.g., Coles et al. 1978; Celnikier et al. 1987; Manoharan 1993; Asai et al. 1998).

## 2.2. The Temporal Power Spectrum

From the Fourier transform of the time-series of the intensity fluctuations one can derive the temporal power spectrum of the scintillations, P(f). If  $C_{\delta n_e}^2(R)$  is the scattering level of the solar wind and  $\Phi_{\delta n_e}(\kappa, z)$  the spatial spectrum of density turbulence, where  $\kappa$  is the spatial wavenumber, and the line of sight to the source is along the z direction, then P(f) can be given by (e.g., Armstrong & Coles 1978; Manoharan & Ananthakrishnan 1990),

$$P(f) = (2\pi r_e \lambda)^2 \int_{\text{observer}}^{\infty} \frac{\mathrm{d}z}{|V_p(z)|} \int_{-\infty}^{+\infty} \mathrm{d}\kappa \ C_{\delta n_e}^2(R) \times \Phi_{n_e}(\kappa, z) \times F_{\text{filter}}(\kappa, z) \times F_{\text{source}}(\kappa, z) \,. \quad (1)$$

In this equation,  $\lambda$  is the observing wavelength and  $r_e$  is the classical electron radius. The transverse velocity  $V_p(z)$  is in the orthogonal x-y plane. Since the drift rate of density irregularities across the line of sight to a radio source causes intensity fluctuations on the ground, the transverse speed,  $V_p(z)$  and the spatial wavenumber,  $\kappa$ , are related to the temporal frequency by  $2\pi f = \kappa \times V_p(z)$ . Thus the width of the temporal power spectrum is directly proportional to the projected speed of the density irregularities perpendicular to the line of sight (Manoharan & Ananthakrishnan 1990).

The Fresnel propagation filter,  $F_{\rm filter}(\kappa,z)=4\sin^2(\kappa^2z\lambda/4\pi)$ , attenuates for wavenumbers  $\kappa_f\lesssim\sqrt{(2\pi/\lambda z)}$ , but does not alter the shape of the temporal power spectrum at large wavenumbers (i.e., at small spatial scale lengths,  $1/\kappa < 1/\kappa_f$ ) (Manoharan et al. 1994; Manoharan et al. 2000). In Equation (1), the integration includes density irregularities of all scale sizes present in the turbulent medium. As the square root of the integral of the temporal power spectrum  $(\sqrt{\int P(f)\,\mathrm{d}f})$  equals the rms of the intensity fluctuations, it can also be normalized by the mean intensity of the source,  $<\mathrm{I}>$ , to yield the scintillation index, m (Manoharan 1993). At a given heliocentric distance, a compact source scintillates more than an extended one and its brightness distribution,  $F_{\mathrm{source}}(\kappa,z)$ , not only causes an overall reduction in scintillation but also attenuates the high-frequency end of the power spectrum

representing scales much smaller than the Fresnel radius (Coles 1978; Manoharan & Ananthakrishnan 1990).

In the case of IPS caused by the solar wind, the scattering power falls steeply with distance from the Sun,  $C_{\delta n_e}^2(R) \propto R^{-4}$  (Manoharan 1993), while the spatial spectrum of density irregularities has a power-law form,  $\Phi_{\delta n_e}(\kappa) = \kappa^{\alpha}$ , with a dissipative scale size (i.e., inner scale or cut-off scale size). Due to the directional flow of plasma, the electron density spectrum can be anisotropic, reflecting the anisotropy in the associated turbulence, leading to considerable deviation from the scintillation properties of an isotropic distribution,  $\Phi_{\delta n_e}(\kappa) = \left(\kappa_x^2 + \frac{\kappa_y^2}{AR^2}\right)^{\alpha/2}$ , where AR is the axial ratio of the density irregularities (e.g., Armstrong et al. 1990; Yamauchi et al. 1998). The three-dimensional power-law index,  $\alpha$ , varies around the "Kolmogorov" value of  $\alpha = -11/3$ , within the range of -2.5 to -4, depending upon the heliocentric distance of the solar wind that is probed and its source region on the Sun (e.g., Coles & Harmon 1989; Manoharan et al. 1994; Yakovlev & Pisanko 2018).

## 2.3. Scintillation by a Comet Plasma Tail

For scintillations produced by a comet plasma tail, the thickness of the turbulent screen is determined by the effective path length through the tail where the line of sight to the source crosses it. Naturally, the line of sight also includes scattering associated with the ambient solar wind along its path. For weak scattering, the variances of comet-tail and solar-wind scintillations simply add, i.e., their power spectra sum. As the solar-wind scattering falls off rapidly with distance from the Sun  $(C_{\delta n_e}^2(R) \propto R^{-4})$ , for a large solar elongation of the source, the effect of the solar wind on the observed scintillation will be less significant and the contribution from the comet ion tail dominates the measured scintillation. For a comet tail, the rate of intensity fluctuation is determined by the concentration of plasma in it and the transverse velocity of the irregularities. The shape of the temporal power spectrum is the combined effect of the flow speed of the plasma away from the nucleus, the irregularity scale sizes, and the level of scattering power. In the present study, the comet was located at distances of  $\gtrsim 2$  AU from the Earth, for which the associated size of the Fresnel radius is about 40% larger than that expected for the solar-wind scintillation. Since the low-frequency part of the temporal spectrum is determined by the effect of large-scale plasma irregularities close to the Fresnel radius, in the present case, the plasma associated with the comet tail is expected to move the Fresnel knee toward the low temporal frequencies, and to increase the scintillation at the low-frequency part of the spectrum.

# 3. THE ORBIT OF COMET 2I/BORISOV AND THE SELECTION OF OCCULTATION SOURCES

The path of Comet 2I/Borisov from mid-October to mid-December 2019 is shown in Figure 2. For each day, the orbit of the comet was obtained with a time resolution of 30 min from the "Solar System Dynamics Group, Horizons On-Line Ephemeris System", provided by the Jet Propulsion Laboratory (http://ssd.jpl.nasa.gov/). During this period, the Sun-comet and Earth-comet distances lay between 2.5 - 2.0 AU and 2.9 - 2.4 AU respectively.

In Figure 2, the positions of the radio sources selected for observation as the plasma tail of the comet passed over them are also marked along the path of the comet. These sources were selected from the Texas and Molonglo catalogs at 365 and 408 MHz (Large et al. 1981; Douglas et al. 1996), respectively, plus the results of IPS measurements made with the Ooty Radio Telescope at 327 MHz (i.e., Manoharan 2009; Manoharan 2012). Since only limited information was available on the length and width of the comet plasma tail, we selected sources in the sky plane whose lines of sight passed within  $\sim 12 \times 12$  arcmin of the coma of the comet, namely B0957+142, B1019+083, B1023+067, and B1129-202, located on the tail side of the comet on 20 and 31 October, 03 November, and 11 December 2019 respectively. The observations of the first 3 sources were made with the Arecibo 305-m Telescope, while B1129-202 was observed with the Green Bank 100-m Telescope.

Previous extensive monitoring of IPS for sources B0957+142 (4C14.35) and B1023+067 (3C243) was available from the Ooty Radio Telescope, operating at 327 MHz (Swarup et al. 1971; Manoharan et al. 1995; Manoharan 2009). For example, a large number of IPS observations of B0957+142, nearly 300 observations between 1992 and 2016 at different elongations, allowed estimates of a scintillation

component size,  $\Theta \approx 150$  mas, and flux density,  $\Delta S \approx 700$  mJy. B1023+067 was monitored about 100 times between 1989 and 2016, these observations providing  $\Theta \approx 100$  mas and  $\Delta S \approx 600$  mJy.

For the solar wind monitoring at Ooty, strong sources ( $S_{327} \gtrsim 2$  Jy) were mostly employed and compact component details were not available for the weak sources B1019+083 and B1129-202. However, after the present comet observations, we requested IPS observations at Ooty and observed B1019+083 during July 2020 and October 2021 (Section 4.1, Figure 3). We did not get an opportunity to similarly observe B1129-202. The parameters of these sources are listed in Table 1, which also summarizes some of the relevant observational parameters.

## 4. OBSERVATIONS, DATA ANALYSIS AND RESULTS

# 4.1. Ooty Control IPS Observations of B1019+083 at 327 MHz

To provide detailed information on B1019+083 at P-band (302-352 MHz) (also illuminating the situation at 1400 MHz), 327-MHz IPS observations were requested with the Ooty Radio Telescope (ORT; Swarup et al. 1971), when the source approached and receded from the Sun. These were made during 14-20 July 2020 and 06-07 October 2021 respectively. The solar elongations of these observations ranged between 36° and 43° (i.e., corresponding to a solar radial offset range of 0.57–0.67 AU). On each day, on-source and off-source data were collected for about 15 and 5 min respectively, along with the observation of a flux-density calibrator. The observational method and data analysis procedures followed are given in Manoharan (1993) and Manoharan et al. (2000). The Ooty temporal power spectrum at  $\lambda = 0.92$  m, in the frequency range of  $f \approx 0.1 - 25$  Hz, includes spatial wavenumbers in the range  $0.002 < \kappa = \frac{2\pi f}{V} < 0.2 \text{ km}^{-1}$ , corresponding to solar-wind density turbulence scales between 5 and 500 km for a typical solar wind velocity of 350 kms<sup>-1</sup>, and the angular size of the source,  $\Theta$  (FWHM) >400 milliarcsec (mas), heavily attenuates the scintillation. During these observations, 2 days were affected by interference. Power spectra of the other 7 days are shown in Figure 3, each in a different color. The solar elongation of each day's observation is also indicated. At such large elongations, the line of sight to the radio source lies close to the ecliptic plane and the solar wind properties would be those of low heliographic latitudes. The figure also contains an IPS model spectrum obtained from Equation 1. This model was computed for a solar wind speed, V = 350 km/s, a source size,  $\Theta = 50$  mas, and a power-law index,  $\alpha = -3.3$ . Moreover, the average model fit to the observed power spectra provides an estimate for the source size of  $\Theta = 50\pm25$  mas, and solar wind speeds in the range of 300 to 400 kms<sup>-1</sup>, which is consistent with the near-Earth in-situ measurements of the solar wind speed in the periods 12–25 July 2020 and 4–9 October 2021 (https://cdaweb.gsfc.nasa.gov). Additionally, the observed average scintillation index,  $m \approx 0.3$ , corresponds to a flux density of the compact component,  $\Delta S \approx 500 \text{ mJy at } 327 \text{ MHz}.$ 

# 4.2. Observations, Data Analysis and Results at Arecibo

IPS measurements were made 50 years ago with the Arecibo Telescope, chiefly to identify sources with sub-arcsecond structure (e.g., Cohen et al. 1967; Cohen & Gundermann 1969; Harris 1973). Recently, exploiting the post-1990s expanded frequency coverage of the telescope, (300 MHz – 10 GHz), IPS observations were recommenced at Arecibo to study the characteristics of turbulence in the solar-wind plasma at a range of distances from the Sun. A full suite of analysis and display programs have been developed for these new measurements (Manoharan et al. 2021).

The present study of Comet Borisov used two of the 305-m Telescope receivers, the so-called "P-Band" and "L-Band Wide" systems, covering the frequency ranges of 302-352, and 1120-1730 MHz respectively. The gains are ~10 K/Jy, with both receivers, recording both orthogonal polarizations. The FPGA-based Mock spectrometer system was used in single-pixel mode (see <a href="http://www.naic.edu/~astro/mock.shtml">http://www.naic.edu/~astro/mock.shtml</a>) to record the data. At P-Band, a single Mock-spectrometer box was employed. This recorded 53.3-MHz bandwidth of dual-polarization data centered at 327 MHz, with each polarization divided into 1024 channels, and having an integration time of 2 msec. At L-band, all 7 available Mock boxes were employed, each processing an 80-MHz bandwidth of dual-polarization data. The bands were centered at 1160, 1240, 1320, 1400, 1480, 1620 and 1700 MHz.

Here, each band was divided into 2048 channels per polarization, with the data being sampled at an integration time of 1 msec.

The occulted sources were tracked for  $\sim 2-2.5$  hours. Off-source data were taken before and after the on-source scans by moving the telescope pointing east of the source by  $\sim 3$  min in right ascension and were useful to compute the source deflection, which also included the system gain variation. Bandpass correction was applied to every 10 sec of data (see https://www.naic.edu/ $\sim$ phil/masdoc.html). Each 80-MHz band at L-band was split into  $8\times 10$ -MHz subbands, with each subband having 256 channels. Individual bad channels within each subband were identified by their high transient rms values ( $>3\sigma$ ) and flagged. For each subband, the frequency-averaged spectral density over the remaining good channels was then calculated for each 1-msec sample, resulting in total-power time series for  $56\times 10$ -MHz subbands of L-band data. These were computed for on- and off-source scans. For the P-Band observations, total-power time series for  $5\times 10$ -MHz subbands were similarly computed.

Running means of 10-sec duration were subtracted from the data streams to remove any slow variations at frequencies below 0.1 Hz, Fourier transforms performed and temporal power spectra computed for 1-min blocks of data for each 10-MHz subband. (The above running mean subtraction is also useful to remove any low-frequency system variations, if present, and/or the response of the slow drifting of a 'screen' (e.g., ionosphere) located close to the observer. However, it will not alter the faster intensity fluctuations generated by the plasma tail.) Average 1-min power spectra were obtained for P- and L-band by averaging all subbands and used for the scintillation index calculation. For display purposes, 2-min spectra were computed for L-band to improve the stability of the spectrum. At high temporal frequency, >10 Hz, the spectrum dropped to the level of the receiver system noise, a constant level independent of frequency. This was subtracted from the on-source power spectrum to obtain the spectrum of the pure intensity fluctuations. However, in the noise-level subtracted spectrum, the fractional error increased monotonically as the scintillation power approached the system noise (Figure 7(a), spectrum shown in 'black'). In order to achieve a nearly constant fractional error over the usable region of the spectrum, the frequency resolution at <0.5 Hz was retained at  $\sim0.1$  Hz, while at higher frequencies adjacent points were averaged, with the number of points averaged increasing such as to keep the spectral points equispaced on the logarithmic scale of the frequency axis (Figure 7(a), spectrum shown in 'red').

# 4.2.1. The Central Occultation of B1019+083 on 31 October 2019

Figure 4 shows the path of the comet on 31 October 2019 with respect to the target source B1019+083, projected on to the plane of the sky. The arrow indicates the direction to the Sun, while the thin-dotted line connects the comet nucleus and the Sun at 12 UT. On 31 October, the solar elongation of the source was 64°, corresponding to a solar offset of 0.9 AU.

At P-band (i.e., 302-352 MHz), the source was observed for about one hour from  $\sim$ 11:10 UT. During this time, the perpendicular angular separation between the center of the comet tail and the line of sight to the source decreased from about 2.5 to 1.5 arcmin. The P-band temporal power spectra did not show any significant change with time as the line of sight to the source approached the plasma tail of the comet. The scintillation index values computed from the power spectra of 1-min data stretches (i.e.,  $m = \sqrt{\int P(f) \, \mathrm{d}f} / \langle I \rangle$ ) are plotted in Figure 5. The error bar shown on each point is the 'peak-to-peak' variation of 5 scintillation indices obtained from the 5 individual subbands, each of 10-MHz width. The rather steady, low level of signal fluctuation seen throughout the entire hour spent at P-band suggests that at a distance of  $\sim$ 3-4×10<sup>5</sup> km from the nucleus of the comet, the detectable width of the tail was  $\lesssim$ 3 arcmin.

Between  $\sim 12:25$  and 13:20 UT, B1019+083 was observed with the L-band system. During this time, the angular separation between the axis of the comet tail and the line of sight to the radio source decreased from  $\sim 1$  arcmin ( $\sim 10^5$  km), with the central part of the tail expected to occult the line of sight at around 13 UT. For each 1-min spectrum, the scintillation index was computed as detailed above. Figure 6 shows the scintillation index as a function of time, reaching a maximum at  $\sim 13$  UT. After this time, the apparent scintillation decreased. However, the source had reached the tracking limit of the telescope, and the telescope pointing moved quickly away from the source (i.e., within less

than 15 s of time, corresponding to the size of the beam at L-band), with the fluctuation level rapidly dropping to a steady low value. By 13:04 UT, the source had moved right out of the telescope beam, and on to a source-free region of the sky, providing a representative baseline of system noise.

## 4.2.2. The Evolution of the L-Band Power Spectra of B1019+083 During its Occultation

When the L-band temporal power spectra of B1019+083 were examined carefully, a systematic evolution could be seen in the spectral shape and integrated power as the line of sight to the source approached the central part of the plasma tail (see Figure 6). Figure 7(a) displays the spectrum observed at ~12:53 UT, approaching the peak seen in Figure 6, after subtracting the off-level of the spectrum corresponding to the level of system white noise. In the spectrum shown in 'black', adjacent pairs of points have been averaged, whereas in the 'red' plot averaging is such that the points are nearly equispaced on the logarithmic scale. Figure 7(a) also includes two model spectra computed for a spherically diverging solar-wind velocity of 360 km/s at a solar elongation of 64° using Equation (1). The 'green' spectrum is for a power-law exponent,  $\alpha = -2.7$ , while the 'blue' spectrum corresponds to  $\alpha = -3.3$ . In contrast, if two different velocity fittings are considered separately for the low- and high-frequency parts of the resultant spectrum, then its high-frequency part would scale to an abnormal high velocity, >2000 km/s. The displayed model spectra adopt an angular source size of  $\Theta = 50$  mas and an anisotropy parameter, AR = 1.5. The derived spectrum from the observations shows the narrowing at the low-frequency part, caused by the large Fresnel scales at a distance of ~2 AU for the plasma screen.

Moreover, comparing the spectra from the beginning of the L-band observations with those near the peak of the scintillation (see Figure 7(b)) shows remarkable changes. The high-frequency part of the spectrum becomes prominent as the central axis of the tail is approached, indicating the presence of small-scale density structures as well as an increase in the scattering power near the central axis of the plasma tail. Figure 7(b) displays 2-min average spectra corresponding to, (i) the start of the L-band observations at  $\sim 12.26$  UT, (ii) close to the peak of the scintillations at  $\sim 12.57$  UT, and (iii) at  $\sim 13:17$  UT, when the telescope pointing lay outside of the plasma tail and at an off-source region. In this figure, UT times are marked on the spectra. Both recent and earlier IPS observations at Arecibo have demonstrated that the L-band scintillation index of selected compact radio sources (e.g., 3C237 and 3C138) drop by a factor of  $\sim 30$  between a peak value at  $\sim 0.07$  AU and a solar offset of 0.9 AU (e.g. Cohen & Gundermann 1969; Manoharan et al. 2021), corresponding to a reduction in spectral power of  $\sim 15$  dB; the solar elongation of the present observations correspond to a solar offset for the line of sight of  $\sim 2$  AU. When the line of sight to the radio source lay close to the center-line of the tail, the power spectrum – plotted in "red" in Figure 7(b) – became broad, extending up to  $\sim$ 10 Hz, and its amplitude increased. This suggests increased scattering when the central part of the tail was approached. At frequencies above 10 Hz, the spectrum merges with the white-noise. Below 4 Hz, the spectrum indicates a power-law of slope  $\alpha \approx -3$ . A further prominent feature seen in the temporal power spectrum is that excess scattering power exists in the 4-9 Hz region. Similar results have been obtained for the solar-system comets, Schwassmann-Wachmann 3-B and Austin (Roy et al. 2007; Salter & Manoharan 2019). This excess power seems to decrease with offset of the line of sight from the center of the tail. The power spectrum derived at  $\sim 12.26$  UT, shown in "blue" in Figure 7(b), corresponding to the start of the L-band observation when the line of sight was at the edge of the plasma tail, shows a similar, but relatively smaller, excess power. When the beam drifted away from the target radio source, the spectrum, shown in "green" in Figure 7(b), contained insignificant power and was essentially flat.

In order to have comparison data, B1019+083 was observed again for a short time at L-band on 05 November 2019. The equivalent temporal power spectrum from this control observation is plotted in "black" in Figure 7(b). This spectrum is nearly flat over the full range of temporal frequencies, at a solar elongation of  $69^{\circ}$ .

## 4.2.3. The Arecibo Observations of Two "Near-Occulatations"

Two other radio sources, B0957+142 and B1023+067, (both established IPS sources at 327 MHz, see Table 1), were also observed at Arecibo on 20 October and 03 November 2019 respectively. As

for B1019+083, both were observed consecutively at P-band (302–352 MHz) and L-band (1120–1730 MHz) for about an hour at each frequency during their individual Arecibo meridian transits. Both sources are fairly strong, the sizes of their compact components being  $\sim 100-150$  mas, (see Table 1). The data analysis was performed as described above, and the 1-min temporal power spectra were computed for both days. Their derived spectra were nearly flat with no excess signal fluctuations being apparent.

The sources were located at angular distances of  $\sim 10$  arcmin from the comet coma in the tail direction. Moreover, since the actual tail occultation times on the above days fell slightly outside of the tracking limit of the telescope, these sources were observed when the lines of sight were separated from the central part of the tail by an orthogonal distance of  $\sim 6$  arcmin. While the non-detection of scintillations could indicate that the tail length was <10 arcmin from the comet coma, corresponding to a radial distance of  $\sim 8 \times 10^5$  km, the plasma tail was possibly longer than 10 arcmin, but sufficiently narrow that the occultations only began after the sources had set at Arecibo.

## 4.3. A Central Tail Occultation Observed with the GBT

On 11 December 2019, just after the perihelion passage of Comet 2I/Borisov, we observed its ion tail occultation of the radio source B1129–202 using the 100-m Green Bank Telescope (GBT) and its PF1\_800 receiver at 820 MHz. The solar elongation of the source was 77°. The source was located at an angular separation of  $\sim$ 12 arcmin ( $\sim$ 10<sup>6</sup> km) from the Comet Borisov nucleus in the anti-solar direction. Figure 8 displays the path of the comet on that day, as projected on the plane of the sky, with the position of B1129–202 shown on the plot. The arrow indicates the direction to the Sun, while the thin-dotted line connects the comet nucleus and the Sun at 11 UT. It is to be noted that this radio source is relatively weak, its interpolated flux at 820 MHz being 0.37 Jy, with a spectral index of  $\sim$ 0.83 between 76 and 4850 MHz using flux densities from VizieR, brought on to the flux-density scale of Baars et al. (1977). There is no a priori information available on the existence of any compact component that this source may contain. (Since the number of radio sources occulted by the plasma tail was limited, we included all possible occultation sources to the observation list, irrespective of their angular sizes, with an additional aim of detecting the rare event of tail detachment, if such were to occur.) Starting from 09:22 UT, the source was observed for about 4 hr. The central part of the tail was expected to cross the line of sight to the source at  $\sim$ 11 UT.

# 4.3.1. Observations, Data Analysis and Results at Green Bank

While the telescope tracked the radio source B1129–202, two backends simultaneously recorded data in two different acquisition modes. These were: (i) the GUPPI pulsar backend (see https://safe.nrao.edu/wiki/bin/view/CICADA/GUPPISupportGuide), recording total-intensity (I), dynamic spectra in pulsar-search mode with 2048 channels over a bandwidth of 200 MHz every 1-msec, and (ii) the VEGAS spectrometer (see https://www.gb.nrao.edu/vegas/), recording spectra of the orthogonal linear polarizations (XX & YY) with 32768 channels over a 187.5-MHz bandwidth every 100 msec. Each "scan" was of 58 min duration. Before each scan, the total-power level of the entire signal chain was re-adjusted. Four such scans were made beginning at 09:22 UT, with the fourth scan lasting only about 30 min. However, due to initial set-up issues, VEGAS recording began only from the second scan at 10:26 UT.

this extended "downward excursion", and the quasi-periodic interference from the cryogenic pump, were also seen in the Stokes-I time series of the GUPPI data. Hence for the GBT data, only the signal from the VEGAS XX polarization was utilized for further analysis.

Data analysis at Green Bank proceeded as follows:

- 1 For all three scans recorded by VEGAS, average XX-polarization spectra were visually inspected, and channels that were heavily RFI-affected were noted. From this, six independent 10-MHz wide frequency ranges were selected that were essentially RFI-free.
- 2 A fifth-order polynomial fit was made to each 58-min (and  $\sim 30$  min for the final scan) scan-averaged spectrum, using just the data within the 6  $\times$  10-MHz RFI-free bands to construct an average bandpass spectrum.
- 3 For each 0.1-sec VEGAS XX-polarization data sample, the recorded spectrum was normalized by the average bandpass spectrum (obtained from step #2), and the  $6 \times 10$ -MHz spectral bands were each averaged in frequency to create  $6 \times$  total-power, 10-MHz bandwidth, continuum time series.
- 4 From these time series, for every 2 min, temporal power spectra were computed, and averaged over the six independent frequency sets. This produced final temporal power spectra, (effectively averaged over 60 MHz). This avoided band-width smearing of possible scintillation effects had we just produced a simple 60-MHz band-width averaged time series before calculating the corresponding power spectra.
- 5 Finally, measuring the area under these power spectra between temporal frequencies of 0.1 and 0.9 Hz, (thus avoiding the effects of the cryogenic pump, very low-frequency contamination caused by any low-level ionospheric scintillation and/or slow drifts), provided a measure of the power contained in fluctuations that could be caused due to non-instrumental effects.

The measured fluctuation power,  $\int P(f) df$ , is shown plotted against time in Figure 9. This shows no significant change during the first 2 hr during which the VEGAS data was acquired, the time during which the cometary ion tail had been predicted to occult the background radio source. However, the final, shorter, 30-min scan indicates a sudden increase in the "fluctuating power". In respect of this, we note that on Dec 11 2019 the Sun rose at Green Bank at 12:26 UT, exactly 2 min after the start of that scan. We conclude that solar emission in the far sidelobes of the antenna could possibly have caused the sudden increase in fluctuations registered in the time-series, rather than this being due to scintillations of the source emission caused by the ion tail of the comet.

For a single polarization, with a 60-MHz bandwidth, total-power channel, sampled at 0.1 sec, the GBT 800-MHz receiver (with a System Equivalent Flux Density (SEFD) of 10 Jy) would theoretically yield a rms noise of (SEFD/ $\sqrt{\beta\tau}$ ) ~ 4.1 mJy. Any fluctuations in excess of about 5 × this noise would be expected to be caused via a physical process such as IPS, (or maybe ionospheric scintillation for time scales on the order of 10's of sec). At a given solar elongation, the scintillation of a source is detectable when its compact component flux density is at least ~20 mJy (Manoharan et al. 1995).

The occultation observation of B1129-202 with the GBT on 11 December 2019 and the control observation on 04 January 2020, respectively at solar elongations 77° and 99°, showed the integrated scintillation spectral power, at frequencies below 1 Hz, equivalent to a flux density of about 20 mJy. From the 2.5-arcsec resolution image at 3 GHz of the Very Large Array Sky Survey (VLASS; Gordon et al. 2021), B1129-202 is seen to consist of a pair of diametrically opposed lobes with hotspots at their outer edges, and similar intensities. Given the lack of significant central component, the IPS that we detect has to come from compact structure in these hotspots, which are separated by 1.3 arcmin, about one-tenth of the GBT's half-power beamwidth. However, in view of the lack of increased signal fluctuations at the anticipated time of the occultation, the quasi-coincidence between the apparent increase in the level of fluctuations and sun-rise at  $\sim$ 12:26 UT, we refrain from using the GBT data from further discussion here.

## 5. DISCUSSION AND SUMMARY

Scintillations of the radio emission from the source B1019+083 seen through the plasma tail of interstellar Comet 2I/Borisov were detected at Arecibo at 1400 MHz on 31 October 2019. At that epoch the radio source had an angular separation from the comet nucleus of 5 arcmin,  $\sim 4 \times 10^5$  km, in the anti-solar direction.

Several other studies had earlier been successful in detecting scintillations of the emission of compact radio sources seen through the plasma tails of solar-system comets at a variety of observing frequencies, (e.g. Ananthakrishnan et al. 1975; Alurkar et al. 1986; Hajivassiliou & Duffett-Smith 1987; Slee et al. 1990; Roy et al. 2007). All have involved short transit times for the compact radio sources through the tails, and effectively provide point measurements of the plasma properties of the tails. The density variations inferred from the excess scintillations caused by the plasma tails have covered a range of rms densities of  $\sim 1-10$  cm<sup>-3</sup>, which were above the values of the background solar-wind density. In the present case, the average solar wind density at the near-Earth orbit was around 5 cm<sup>-3</sup> for the period between 30 October and 15 December 2019 (https://cdaweb.gsfc.nasa.gov), and for a typical spherically symmetrical expansion of the solar wind, this would be lower by about a factor of 4 at the comet distance of  $\sim 2$  AU from the Sun. In respect of a relationship between the density  $(n_e)$ and its fluctuations ( $\delta n_e$ ) in the solar wind, the ISEE-1 and -2 space propagation experiments showed that  $\delta n_e \propto n_e$ , while high-time resolution measurements by the ISEE-3 spacecraft demonstrated that  $n_e \propto \delta n_e^{0.85}$  (Celnikier et al. 1987; Zwickl et al. 1988). In general, since the level of IPS at L-band is lower by an order of magnitude than that at 327 MHz (Manoharan et al. 2021), the excess levels of scintillation observed on 31 October 2019, when the comet was located at a distance  $\sim$ 2 AU, compared with the Ooty IPS (Figure 3), suggest the density enhancement in the plasma tail to be in the range of  $\sim 15 - 20$  times higher than that from the background solar wind.

Figure 10 shows the expected level of scintillation, caused by the rms electron density variations of the background solar wind, along the line-of-sight between the observer and a distance of 3.2 AU. It includes the position of crossing of the plasma tail at 2.4 AU. The continuous curve represents the scintillation weighting function at a solar elongation of 64° for an observing frequency of 1420 MHz, and also includes the effect of an angular source size of 50 mas. The observed scintillation index is the integration of the contribution of  $\delta n_e(z)$  at each point along the line of sight,  $m^2 \sim \int \left[\delta_{n_e}(z)\right]^2 dz$ . The dotted line indicates the maximum contribution by the background solar wind to the observed scintillation index, the excess above this being the scintillation due to the plasma tail of the comet. In Figure 6, it is to be noted that the increase in scintillation between the background solar wind at 0.9 AU (i.e.,  $\epsilon = 64^{\circ}$ ) and near the central axis of the tail is  $\sim$ 4 times or more. However, the scintillation due to the solar wind changes with the solar offset (R), as  $m \sim R^b$  and the radial dependence index b ranges between -1.5 and -1.6 and does not significantly change with the observing frequency (Cohen & Gundermann 1969; Manoharan 1993; Manoharan et al. 2021). Thus a normalization of scintillation of the background solar wind at the distance of the tail would lead to an increase in the integrated  $\delta_{n_e}$  in the range of 15 – 20 times and more.

For the present observations, the contributions of scintillations at 1400 MHz from IPS at the tangential heliocentric distance of  $R \approx 0.9$  AU for radio source B1019+083 on 31 Oct 2019 are expected to be insignificant and they can add little power to the observed temporal spectra. For example, the observed temporal spectra on 31 October were well above the 10 dB level (see Figure 7a), extending to frequencies >4 Hz, and as the line of sight to the source approached the center-line of the tail, additional features are seen at frequencies  $\geq 5$  Hz. When we carefully examine the shape of the spectra derived for the 1400-MHz band at temporal frequencies  $\leq 4$  Hz, (see Figure 7b), the spectral characteristics resemble those of a typical IPS model spectrum, although with a much higher level of scintillation than is expected from IPS. It is likely that the observed spectral shape is the result of scattering caused by two types of prominent plasma density inhomogeneities. In the spectral region below 4 Hz, it is possible that the scintillations are caused by plasma density irregularities via the interaction of the solar wind with the comet coma. The transfer of energy from the solar wind to the cometary coma, though this interaction is an open question (e.g., Brandt 1968; Biermann et al. 1967; Gombosi 2015), causes the comet itself to represent a source of interplanetary plasma which becomes

dominant as the comet approaches the Sun (e.g., Gombosi 2015). In the neighbourhood (or vicinity) of solar-wind interaction, the plasma flow characteristics are largely controlled by the properties of the solar-wind flow, and scintillations resembling those of IPS are scaled to an enhanced level by strong localized density perturbations. In fact, this region of the spectrum below 4 Hz dominates the overall scintillation index, and also displays a well-formed Fresnel knee. It also shows the signature of anisotropy, the 'rounded knee', with axial ratio of  $\approx 1.5$ , possibly influenced by the directed plasma flow (see Figure 7a).

The temporal spectrum also shows broad, prominent spectral features in its high-frequency part,  $\gtrsim$ 5 Hz, in which the contribution from the background solar wind at a solar offset of 0.9 AU is expected to be insignificant for L-band measurements. These are probably caused by density inhomogeneities present in the central part of the plasma tail. The images of Comet 2I/Borisov obtained with the Hubble Space Telescope and by the W. M. Keck Observatory have been examined for 16 November to 09 December, including the image shown in Figure 1. The Hubble Space Telescope also provided images following the comet's perihelion passage on 08 December, after which the size of the dust tail marginally increased. However, as demonstrated by the images of several solar-system comets, the plasma tail is generally well collimated compared to the dust tail, and follows the direction of the interplanetary magnetic field (e.g., Gombosi 2015). The high-frequency spectral features are likely due to one, or a combination, of the following factors: (i) an associated spatial density spectrum much flatter than the Kolmogorov spectrum, (ii) a highly directional flow of plasma, resulting in an anisotropic spectrum, (iii) a high-speed flow, or (iv) strong scattering conditions leading to a broad spectrum. Since the level of scintillation is low and the spectrum is not broadened at its low-frequency part, a strong scattering situation is unlikely (e.g., Manoharan 2010). The gradual changes in the shape of the spectrum, and the high-frequency part becoming prominent as the central axis of the tail is approached, indicate the presence of small-scale density structures near the central axis of the plasma tail. A plasma flow acceleration leading to velocities much higher than those of the solar wind is implausible in the cometary environment, because an overall shift in the spectrum should then be seen. Moreover, if the high-frequency broadening alone is considered to be due to the scaling of velocity, it would relate to an unrealistic flow velocity, >2000 km/s. The presence of magnetic fields, which in general pervade the turbulent interplanetary plasma, and their strong interactions, can ultimately lead to filamentary structures, knots and/or kinks in the plasma tail. Thus, an anisotropic, flat spatial density spectrum can be a possible cause for the broad spectral feature. In Figure 7(a), we show a model spectrum with a flat power-law exponent of  $\alpha = -2.7$  and an axial ratio of 1.5. This demonstrates approximate correlation with the high-frequency part of the spectrum.

Thus, the overall observed power spectrum of the plasma tail of Comet 2I/Borisov likely contains different types of density spectra and shows the presence of density scales in the range of  $\sim 10-700$  km, which are likely associated with the interplanetary environment produced by the comet, plus interaction with the solar wind. Section 4.2.2 discussed the evolution of the spectral shape, as the line of sight to the source B1019+083 approached the central part of the tail (see Figure 7(b)). In particular, the result on the high-frequency excess, corresponding to irregularity scale sizes much smaller than the Fresnel scale, is similar to the previous studies of the two solar-system comets, Schwassmann-Wachmann 3-B and Austin, albeit within 1 AU of the Sun (Roy et al. 2007; Salter & Manoharan 2019). These results suggest the presence of small-scale density structures in the concentrated central part of comet tails.

### ACKNOWLEDGMENTS

The Arecibo Observatory is operated by the University of Central Florida under a cooperative agreement with the National Science Foundation (AST-1822073), and in alliance with Universidad Ana G. Méndez and Yang Enterprises, Inc. The Green Bank Observatory is a facility of the National Science Foundation (NSF) operated under cooperative agreement by Associated Universities, Inc.

The image in Figure 1 has been obtained from the W.M. Keck Observatory, which is operated as a scientific partnership among the California Institute of Technology, the University of California and NASA. We also acknowledge the JPL Solar System Dynamics Group's Horizons On-Line Ephemeris System (http://ssd.jpl.nasa.gov/) for the comet ephemeris data and the Coordinated Data Analysis Web (CDAWeb) service for providing solar wind data (https://cdaweb.gsfc.nasa.gov/).

## REFERENCES

- Alurkar, S. K., Bhonsle, R. V., & Sharma, A. K. 1986, Nature, 322, 439, doi: 10.1038/322439a0
- Ananthakrishnan, S., Bhandari, S. M., & Rao,A. P. 1975, Ap&SS, 37, 275,doi: 10.1007/BF00640353
- Armstrong, J. W., & Coles, W. A. 1978, ApJ, 220, 346, doi: 10.1086/155912
- Armstrong, J. W., Coles, W. A., Kojima, M., & Rickett, B. J. 1990, ApJ, 358, 685, doi: 10.1086/169022
- Asai, K., Kojima, M., Tokumaru, M., et al. 1998, Journal of Geophysical Research: Space Physics, 103, 1991,
  - doi: https://doi.org/10.1029/97JA02750
- Baars, J. W. M., Genzel, R., Pauliny-Toth, I. I. K., & Witzel, A. 1977, A&A, 61, 99
- Bagnulo, S., Cellino, A., Kolokolova, L., et al. 2021, Nature Communications, 12, 1797, doi: 10.1038/s41467-021-22000-x
- Biermann, L., Brosowski, B., & Schmidt, H. U. 1967, SoPh, 1, 254, doi: 10.1007/BF00150860
- Brandt, J. C. 1968, ARA&A, 6, 267, doi: 10.1146/annurev.aa.06.090168.001411
- Celnikier, L. M., Muschietti, L., & Goldman, M. V. 1987, A&A, 181, 138
- Cohen, M. H., & Gundermann, E. J. 1969, ApJ, 155, 645, doi: 10.1086/149897
- Cohen, M. H., Gundermann, E. J., & Harris, D. E. 1967, ApJ, 150, 767, doi: 10.1086/149380
- Coles, W. A. 1978, SSRv, 21, 411, doi: 10.1007/BF00173067
- —. 1995, SSRv, 72, 211, doi: 10.1007/BF00768782
- Coles, W. A., & Harmon, J. K. 1989, ApJ, 337, 1023, doi: 10.1086/167173
- Coles, W. A., Harmon, J. K., Lazarus, A. J., & Sullivan, J. D. 1978, Journal of Geophysical Research: Space Physics, 83, 3337, doi: https://doi.org/10.1029/JA083iA07p03337
- Condon, J. J., Cotton, W. D., Greisen, E. W., et al. 1998, AJ, 115, 1693, doi: 10.1086/300337

- Cordiner, M. A., Milam, S. N., Biver, N., et al. 2020, Nature Astronomy, 4, 861, doi: 10.1038/s41550-020-1087-2
- Douglas, J. N., Bash, F. N., Bozyan, F. A., Torrence, G. W., & Wolfe, C. 1996, AJ, 111, 1945, doi: 10.1086/117932
- Gombosi, T. I. 2015, in Geophysical Monograph Series, Vol. 207, Magnetotails in the Solar System, ed. A. Keiling, C. Jackman, & P. Delamere, 169–188, doi: 10.1002/9781118842324.ch10
- Gordon, Y. A., Boyce, M. M., O'Dea, C. P., et al. 2021, ApJS, 255, 30, doi: 10.3847/1538-4365/ac05c0
- Hajivassiliou, C. A., & Duffett-Smith, P. J. 1987,MNRAS, 229, 485,doi: 10.1093/mnras/229.3.485
- Harris, D. E. 1973, AJ, 78, 369, doi: 10.1086/111425
- Hewish, A., Scott, P. F., & Wills, D. 1964, Nature, 203, 1214, doi: 10.1038/2031214a0
- Kojima, M., & Kakinuma, T. 1987,J. Geophys. Res., 92, 7269,doi: 10.1029/JA092iA07p07269
- Large, M. I., Mills, B. Y., Little, A. G., Crawford,
  D. F., & Sutton, J. M. 1981, MNRAS, 194, 693,
  doi: 10.1093/mnras/194.3.693
- Manoharan, P. K. 1993, SoPh, 148, 153, doi: 10.1007/BF00675541
- Manoharan, P. K. 2009, in Astronomical Society of the Pacific Conference Series, Vol. 407, The Low-Frequency Radio Universe, ed. D. J. Saikia, D. A. Green, Y. Gupta, & T. Venturi, 359
- Manoharan, P. K. 2010, in Magnetic Coupling between the Interior and Atmosphere of the Sun, ed. S. Hasan & R. J. Rutten (Berlin, Heidelberg: Springer Berlin Heidelberg), 324–331
- —. 2012, ApJ, 751, 128,doi: 10.1088/0004-637X/751/2/128
- Manoharan, P. K., & Ananthakrishnan, S. 1990,Mon. Not. R. Astron. Soc., 244, 691

- Manoharan, P. K., Ananthakrishnan, S., Dryer,
  M., et al. 1995, Solar Physics, 156, 377,
  doi: 10.1007/BF00670233
- Manoharan, P. K., Kojima, M., Gopalswamy, N., Kondo, T., & Smith, Z. 2000, Astrophys. J., 530, 1061, doi: 10.1086/308378
- Manoharan, P. K., Kojima, M., & Misawa, H.1994, J. Geophys. Res., 99, 23411,doi: 10.1029/94JA01955
- Manoharan, P. K., Perillat, P., & AO Team. 2021, in American Astronomical Society Meeting Abstracts, Vol. 237, American Astronomical Society meeting Abstracts #237, 405.05
- Manoharan, P. K., Tokumaru, M., Pick, M., et al. 2001, ApJ, 559, 1180, doi: 10.1086/322332
- Manzini, F., Oldani, V., Ochner, P., & Bedin,L. R. 2020, MNRAS, 495, L92,doi: 10.1093/mnrasl/slaa061
- Roy, N., Manoharan, P. K., & Chakraborty, P. 2007, ApJL, 668, L67, doi: 10.1086/522780

- Salter, C., & Manoharan, P. K. 2019, BAAS, 51, 116
- Slee, O. B., Bobra, A. D., Waldron, D., & Lim, J. 1990, Australian Journal of Physics, 43, 801, doi: 10.1071/PH900801
- Swarup, G., Sarma, N. V. G., Joshi, M. N., et al. 1971, Nature Physical Science, 230, 185, doi: 10.1038/physci230185a0
- Yakovlev, O. I., & Pisanko, Y. V. 2018, Advances in Space Research, 61, 552,doi: https://doi.org/10.1016/j.asr.2017.10.052
- Yamauchi, Y., Tokumaru, M., Kojima, M.,Manoharan, P. K., & Esser, R. 1998,J. Geophys. Res., 103, 6571,doi: 10.1029/97JA03598
- Zwickl, R., Hildner, E., Bame, S., Gosling, J., & Sofaly, K. 1988, EOS, 69, 1358

Table 1. Occultation Radio Sources Parameters

Src Name	RA(B1950)	Dec(B1950)	$S_{327}$	$S_{820}$	$S_{1400}$	$\Delta S_{327}/\Theta$	Date (2019)	$\epsilon$	$D_{\mathrm{probe}}$	Obs
	hh:mm:ss.s	dd:mm:ss.s	Jy	Jy	Jy	$\mathrm{mJy/mas}$	(UT range, hh:mm)	(deg)	$\mathrm{km}$	
B0957+142	09:57:45.9	+14:16:00.2	3.5	-	1.17	700/150	20 Oct (11:16-13:55)	71	$8 \times 10^{5}$	AO
B1019+083	10:19:12.5	+08:23:42.0	1.7	_	0.61	500/50	31 Oct (11:03-13:21)	64	$4{\times}10^5$	$AO^c$
B1023+067	10:23:55.1	+06:42:50.5	4.3	_	0.85	600/100	03 Nov (11:02-13:09)	63	$8 \times 10^5$	AO
B1129-202	11:29:44.4	-20:17:17.8	0.8	0.37	0.13	_	11 Dec (09:15-13:15)	77	$\sim 10^6$	$\mathrm{GBT}^c$

 $S_{327}$  and  $S_{1400}$  - source flux densities at 327 and 1400 MHz, respectively, obtained from the Ooty Radio Telescope (Manoharan 2012) and the NRAO VLA Sky Survey (NVSS) (Condon et al. 1998);  $S_{820}$  - source flux density at 820 MHz derived as described in Section 4.3;  $\Delta S_{327}$  and  $\Theta$  - scintillating flux density and estimated angular size of the compact component obtained from extensive IPS observations of the Ooty Radio Telescope at 327 MHz (Manoharan 2012);  $\epsilon$  - solar elongation of the source;  $D_{\text{probe}}$  - distance between comet nucleus and source line of sight crossing in the tail direction;  $AO^c$  and  $GBT^c$  - Arecibo and Green Bank observations probed the central part of the tail; AO observations made in the 327- and 1400-MHz bands; AO0 observations made in the 820-MHz band.



**Figure 1.** Image of Comet 2I/Borisov taken by the Keck Observatory's Low-Resolution Imaging Spectrometer on 24 November 2019. To illustrate the size scale, an image of the Earth is shown (Credit: P. van Dokkum, G. Laughlin, C. Hsieh, S. Danieli, Yale University).

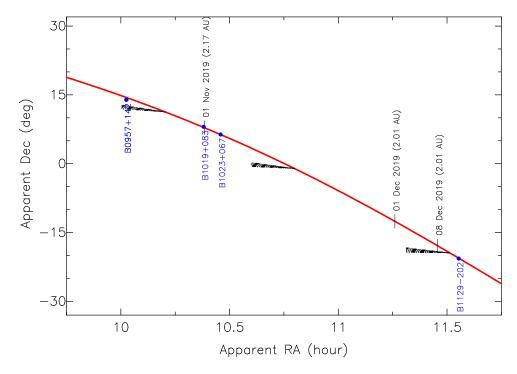


Figure 2. The path of Comet 2I/Borisov from mid-October to mid-December 2019. The heliocentric distances of the comet are marked on 01 November, 01 December, and on the perihelion date 08 December 2019. Typical tail directions along the anti-solar direction are shown. The occultation sources are also plotted along the path of the comet (see Table 1).

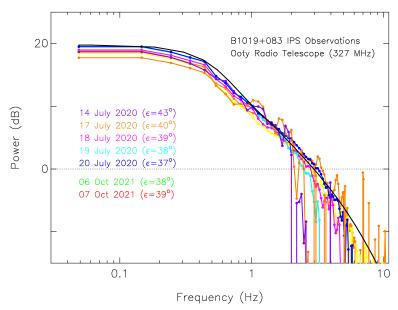
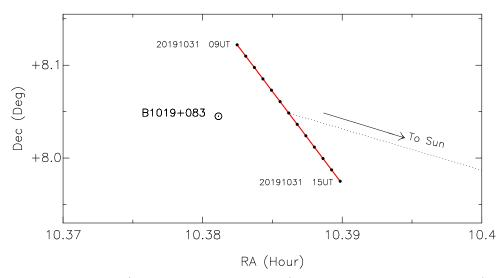


Figure 3. The derived IPS power spectra from observations of B1019+083 after subtracting the noise floor. These spectra were obtained from the Ooty Radio Telescope at 327 MHz. For each spectrum, the date of observation and the solar elongation of the source are shown with the corresponding color code. The horizontal dotted line indicates the typical subtracted level of the white-noise spectrum due to the receiver system noise. A model spectrum for typical solar wind parameters, (spectral power-law index,  $\alpha = -3.3$ , and solar wind speed, V = 350 km/s), and source size,  $\Theta = 50 \text{ mas}$ , is shown as a continuous curve (solid black spectrum).

# Comet Borisov (C/2019 Q4) Path on 31 OCT 2019



**Figure 4.** Path of Comet 2I/Borisov on 31 October 2019 (shown in red between 9 and 15 UT) plotted on the sky plane, with respect to the radio source, B1019+083. The plot axes are coordinates on the date of observation. The thin-dotted line connects the position of the Sun and the comet nucleus at 12 UT, while the arrow indicates the Sunward direction from the comet. As seen in the plot, the central portion of the anti-solar comet plasma tail was expected to cross the line of sight to B1019+083 around 13 UT.

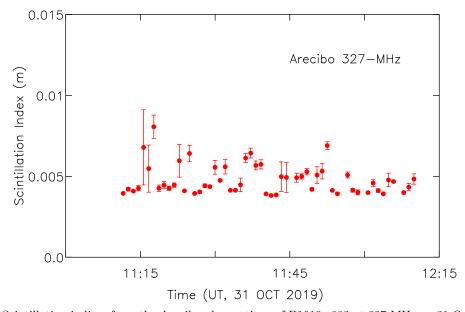


Figure 5. Scintillation indices from the Arecibo observations of B1019+083 at 327 MHz on 31 October 2019. This data set was taken with a bandwidth of  $\sim 50$  MHz and covers a time interval of about 11:10 to 12:12 UT. During this time, the line of sight to the radio source was about 2 arcmin north of the comet tail position. Each point on the plot corresponds to the rms computed by integrating a 1-min temporal power spectrum. Each vertical bar represent the 'peak-to-peak' variation of 5 scintillation indices obtained from the 5 individual subbands of 10-MHz width. The level of the fluctuations remained essentially constant.

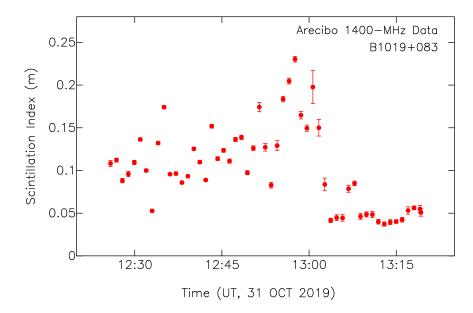


Figure 6. Scintillation indices from Arecibo observations of B1019+083 at L-band on 31 October 2019. Each point corresponds to the rms computed by integrating a 1-min temporal power spectrum. The vertical bars on the points represent the  $\pm 1$ - $\sigma$  uncertainty. In these observations, a wide bandwidth was employed, which helped generate highly sensitive temporal power spectra. The central portion of the comet tail was expected to cross the line of sight around 13 UT. A gradual increase in scintillation was seen from the start of the scan, with the scintillation peaking around 12:58 UT. From about 13:03 UT, the telescope pointing moved off the source and on to "blank sky" away from the target. Thus the plotted points in the time range of 13:04 – 13:18 UT represent observations of a region that provides a typical "off-source" rms level.

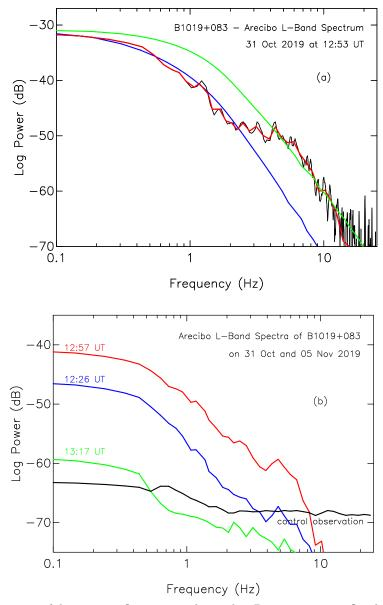


Figure 7. Power spectra of the intensity fluctuations observed on B1019+083 on 31 October and 05 November 2019. The horizontal axis is the temporal frequency (Hz) and the vertical axis is log power (dB). From each spectrum, its corresponding white-noise level has been subtracted. (a): The observed spectra of B1019+083 at 1400-MHz on 31 October, at 12:53 UT plotted in 'black' and 'red' are, respectively, the spectrum with an averaging of two adjacent points, and the same spectrum in which the averaging is such that the points are nearly equispaced on the log scale. For comparison, simple model spectra obtained from Equation (1) are shown. The spectrum shown in 'green' is for a power-law exponent,  $\alpha = -2.7$  and the spectrum plotted in 'blue' is for  $\alpha = -3.3$ . For both model spectra, a spherically symmetric solar-wind velocity of 360 km/s, an anisotropy parameter, AR = 1.5, and a source size of 50 mas are used. (b): The spectra plotted, in red, blue, and green respectively, correspond to 2-min average spectra at  $\sim$ 12:57,  $\sim$ 12:26, and  $\sim$ 13:17 UT (see Figure 6) on 31 October 2019. When the scintillation is at the peak, the spectrum is broad and extends up to about 10 Hz, and its width/shape provides information on the speed and size of density irregularities crossing the line of sight to the radio source. The spectrum shown in black corresponds to a control observation taken on 05 November 2019, when B1019+083 was well away from the tail of the comet at a solar elongation of 69°. It shows the typical background rms level. This spectrum is plotted without subtracting the white-noise level.

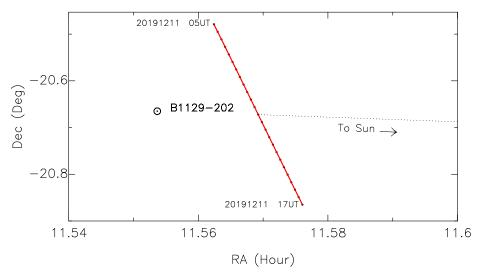


Figure 8. Similar to Figure 4, the comet's path on 11 December 2019, plotted with respect to the radio source B1119-202. The thin-dotted line connects the position of the Sun and the comet nucleus at 11 UT. As seen in the plot, the central portion of the anti-solar comet plasma tail was expected to cross the line of sight to B1129-202 around 11 UT.

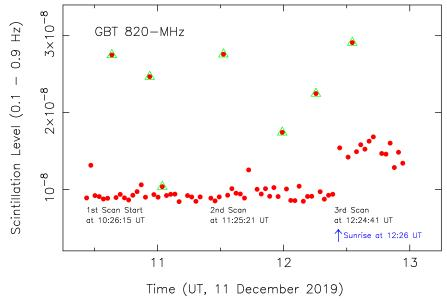
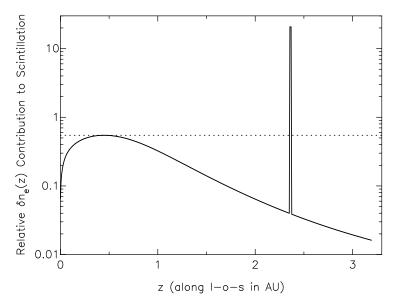


Figure 9. Relative level of fluctuations from the Green Bank Telescope observations of B1129-202 at 820 MHz on 11 December 2019. Each point on the plot corresponds to the rms computed by integrating the  $\sim$ 2-min temporal power spectrum. The central portion of the comet tail was expected to cross the line of sight around 11:00 UT. However, we observed a nearly steady level of fluctuation up to the sunrise at  $\sim$ 12:26 UT, following which an increase in the level of scintillation was observed. The points enclosed by the 'green' triangles are likely affected by interference.



**Figure 10.** The rms electron density contribution of the background solar wind to the level of scintillation at 1420 MHz along the line-of-sight between the observer and a distance of 3.2 AU. The line-of-sight crosses the plasma tail of the comet at 2.4 AU. See Section 5 for details.